Broad-Band Multiple OAMs' Generation With Eight-Arm Archimedean Spiral Antenna (ASA)

YANG YANG [1,3], **YUBIN GONG** [1], **KAI GUO** [2], **FEI SHEN** [3], **JINGHUA SUN** [3], **AND ZHONGYI GUO** [2,3]

[1] National Key Laboratory on Vacuum Electronics, University of Electronic Science and Technology of China (UESTC), Chengdu 610054, China
[2] School of Computer and Information, Hefei University of Technology, Hefei 230009, China
[3] School of Electrical Engineering and Intelligentization, Dongguan University of Technology, Dongguan 523808, China

Corresponding authors: Yubin Gong (ybgong@uestc.edu.cn) and Zhongyi Guo (guozhongyi@hfut.edu.cn)

ABSTRACT In this paper, an eight-arm Archimedean spiral antenna (ASA) is proposed to generate multiple orbital angular momentum (OAM) modes over a respectable frequency band (1.9-3GHz). Firstly, the principle of radiation by eight-arm ASA with right-hand spiral line is analyzed and simulated. It is demonstrated that the OAM modes and polarizations of the generated vortex waves are reconfigurable by changing the fed phases of the eight arms and controlling the radius of the antenna arm. Meanwhile, a prototype is fabricated and measured, in which experimental results agree well with simulation ones. At last, compared with other recently reported OAM-generating antennas, the proposed antenna with the smaller structure ($\Phi 2.45\lambda_0$, where λ_0 is the wavelength of the center frequency) can produce the higher gain (4.5-11.2dBi) vortex waves carrying multiple OAM modes (five modes) in the broad band of 1.9-3GHz.

INDEX TERMS Archimedean spiral antenna (ASA), left-hand circularly polarized (LCP), right-hand circularly polarized (RCP), orbital angular momentum (OAM), vortex wave.

I. INTRODUCTION

Since the quantum characteristics of the orbital angular momentum (OAM) modes were discovered by Allen *et al.* [1] in 1992, OAM has attracted lots of attentions. The electromagnetic (EM) wave carrying OAM has a helical phase structure of $e^{-jl\phi}$, where ϕ is the transverse azimuthal angle, and l represents the topological charge of the OAM mode. Due to the infinite number of OAM modes and the orthogonality between different OAM modes [2], [3], OAM has excellent performances in manipulating particles [4], [5], quantum information processing [6], and communication systems [7]–[12] and imaging systems [13]–[16]. However, no realistic system can ever generate infinite OAM modes. Therefore, in order to further improve the capacity of the communication systems, we should combine OAM multiplexing technology with other multiplexing technologies, such as frequency multiplexing technology. Therefore,

the generation of the broadband vortex waves carrying multiple OAM is of great importance.

As well known, there are several ways to generate OAM waves in radio frequency (RF) domain, such as the helical parabolic antenna [11], the spiral phase plate (SPP) [17], the circularly polarized patch [18], [19], the circular loop antenna [20], the three-dimensional helical antenna [21], the Archimedean spiral antennas [22]–[24], the equiangular spiral antenna [25], metasurface [26], [27] and antenna array [28]. However, these structures have some defects more or less. The helical paraboloid antenna [11], the SPP structure [17] and metasurface [26], [27] may only generate a single OAM mode. The circularly polarized patch [18], [19], the circular loop antenna [20] and the equiangular spiral antenna [25] can just work in a narrow frequency. The helical antenna [21] is difficult to fabricate due to its three-dimensional configuration. The Archimedean spiral antennas [22]–[24] can only radiate different OAM modes at different frequencies, not for the broad-band range. The antenna array is large and expensive [28]. Since all the above methods have the shortcomings of themselves, it is necessary

The associate editor coordinating the review of this manuscript and approving it for publication was Yasar Amin [ID].

to explore an approach with smaller structure and lower cost to generate multiple OAM modes over a respectable frequency band.

In this paper, an eight-arm Archimedean spiral antenna (ASA) is proposed to generate multiple OAM modes in a broad-band range (1.9-3GHz). The outer-fed antenna with smaller structure can generate the same vortex wave as that of the phased antenna array. For the designed right-hand spiral line, by changing the fed phases of the eight arms and controlling the radius of the antenna arm, the left-hand circularly polarized (LCP) vortex waves with OAM modes $l = 0, 1, 2$ and the right-hand circularly polarized (RCP) vortex wave with OAM modes $l = 0, -1, -2$ can be generated in 1.9-3GHz. To validate the performance, simulations are carried out and one demonstrator is developed, fabricated, and measured, in which experimental results agree well with simulation ones. In addition, the performance comparisons of this work to other recently reported OAM-generating antennas demonstrate that the proposed antenna with the smaller structure ($\Phi 2.45\lambda_0$, where λ_0 is the wavelength of the center frequency) can produce the higher gain (4.5-11.2dBi) vortex waves carrying multiple OAM modes (five modes) in the broad band of 1.9-3GHz.

II. THEORETICAL ANALYSIS AND ANTENNA DESIGN

In this section, the designed eight-arm ASA is based on Archimedean curve whose polar coordinate equation can be expressed as $\rho = \rho_0 + \delta(\varphi - \varphi_0)$, where ρ, ρ_0, δ, φ_0 and φ are the radial distance, initial radial distance, spiral constant, initial angle and winding angle, respectively. Therefore, based on the current band theory, the radiation from the ASA comes mainly from an equivalent travelling ring of current with the circumference $(l + 1)\lambda_g$ in the active region, where l and λ_g are the integer and equivalent guided wavelength, respectively. In general, for the observation point $P(r, \theta, \varphi)$ in far-field zone, its field expressions is similar to that of Archimedean antenna, which can be expressed as follows [23]:

$$E_\theta = e^{jl(\alpha+\pi/2)}e^{-jkr}\frac{j60\pi l}{r\tan\theta}J_l(ka\sin\theta) \quad (1a)$$

$$E_\varphi = je^{jl(\varphi+\pi/2)}e^{-jkr}\frac{jk60\pi a}{r}J_l'(ka\sin\theta) \quad (1b)$$

$$E_r = e^{jl(\varphi+\pi/2)}e^{-jkr}\frac{jk60\pi a}{r}\frac{1}{\cos\theta\sin\varphi}$$
$$\cdot [\frac{l\cos\varphi}{ka\sin\theta}J_l(ka\sin\theta) - jJ_l'(ka\sin\theta)\sin\varphi] \quad (1c)$$

where $a = l\lambda_g/2\pi$ is the radius of the active region, $J_l(ka\sin\theta)$ and $J_l'(ka\sin\theta)$ are the Bessel function of the first kind and its derivative, respectively. It can be seen from the above formula that the radiated fields are mainly characterized by the Bessel functions and the phase factor $e^{jl(\varphi+\pi/2)}$, from which the field distributions fit the features of OAM-carrying waves and the number of OAM mode is exactly equal to l.

Moreover, for the eight-arm ASA, there exist seven independent modes [29], and the fed phases of these modes can be given as follows:

$$A_1 = (0, \frac{2\pi}{8}, \frac{4\pi}{8}, \ldots, \frac{2\pi \cdot (8\text{-}1)}{8}) \quad (2a)$$

$$A_2 = (0, \frac{4\pi}{8}, \frac{8\pi}{8}, \ldots, \frac{2\pi \cdot (8\text{-}2)}{8}) \quad (2b)$$

$$\vdots$$

$$A_{8-2} = (0, \frac{2\pi \cdot (8\text{-}2)}{8}, \ldots, \frac{8\pi}{8}, \frac{4\pi}{8}) \quad (2c)$$

$$A_{8-1} = (0, \frac{2\pi \cdot (8\text{-}1)}{8}, \ldots, \frac{4\pi}{8}, \frac{2\pi}{8}) \quad (2d)$$

It is observed that the fed phase arrangements expressed by (2a) and (2d), (2b) and (2c) undergo a left–right flip starting at the second element. Based on the incident and reflected currents travelling along the spiral arms theory in [24], if this out-fed spiral antenna is excited according to the mode 7, it is possible to generate the vortex waves with the opposite circular polarization and OAM mode to that of mode 1. In addition, the spiral circumference is sufficiently smaller than that of the required active region for the mode 7, which is 7λ. Therefore, for the mode 7, the currents will be mainly reflected from the arm origins and travel towards the ends of the spiral arms. Then, they arrive at the active radiation zone for the mode 1, mimicking the case of inner-fed spiral arms. Finally, a radiation similar to the mode 1 but with an opposite polarization and opposite OAM mode can be generated.

Moreover, the working frequency range depends on the circumference range of the spiral arms, and the largest circumference determines the numbers of OAM modes. In order to generate all the OAM modes, the circumference $C = 2\pi r_1$ should be in the length range $[3\lambda_{max}, 5\lambda_{min}]$, where r_1 is the outer radius, λ_{min} and λ_{max} are the minimum and maximum equivalent wavelengths, respectively. Therefore, λ_{max} should be less than $1.67\lambda_{min}$, which means that f_{max} should be less than $1.67f_{min}$, where f_{min} and f_{max} are the minimum and maximum working frequencies, respectively. Therefore, once the radius r_1 is selected as a constant, the frequency range will be determined.

Based on the above discussions, when this spiral antenna with right-handed wire is excited according to the modes 1-3, the LCP vortex waves with topological charges of $l = 0, 1, 2$ can be generated over a respectable frequency band. In contrast, when it is excited according to the mode 5-7, the opposite RCP vortex waves with topological charges of $l = 0, -1, -2$ can be generated over a respectable frequency band.

The geometry of the ASA is presented in Figs. 1 (a-c). It can be seen that the ASA consists of five main parts: the first is the eight Archimedean spiral metal curves which are engraved on the front of the substrate; the second is a 0.762 mm thick Rogers 4350B substrate with a relative permittivity of 3.48 and a dielectric loss tangent of 0.0031; the third is a metal grounding ring printed at the bottom of the substrate, which can also be used for better impedance
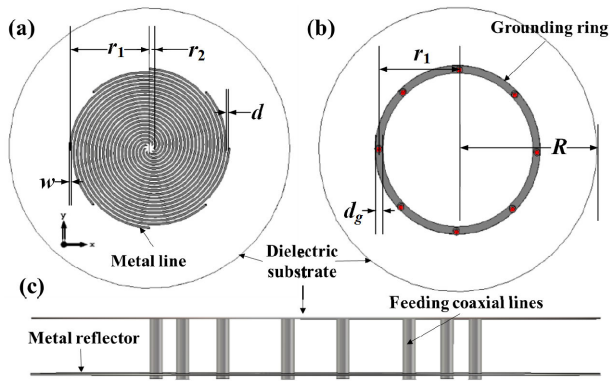
FIGURE 1. The geometry of the proposed eight-arm ASA: (a) the top view of dielectric plate, (b) the bottom view of dielectric plate, (c) the side view of the whole eight-arm ASA.

TABLE 1. Main parameters of the antenna.

Parameter	value
a	$5.09mm/rad$
r_1	$85mm$
r_2	$4mm$
w	$2mm$
dg	$8mm$
d	$2mm$
R	$300mm$

matching; the fourth is the eight feeding coaxial lines; and the last is the metal reflector which is $0.25\lambda_0$ away from the substrate, where λ_0 is the wavelength of the center frequency.

The values of these parameters of the structure in Fig.1 are presented in TABLE 1. The eight spiral curves are evenly spaced on the top of the substrate but with 45degree of phase difference between any two adjacent curves. The inner and outer radius of the spiral curves are $r_2 = 4$ mm and $r_1 = 85$ mm, respectively. Each arm width is $w = 2$ mm. Each arm growth rate of the spiral is $a = 5.09$mm/rad. The number of turns is $N = 2.5$. Therefore, the space between any two adjacent curves is $d = 2$ mm. The radius of the grounding ring is also $r_1 = 85$ mm and its width is $dg = 8$ mm. The same radius of the reflector and the substrate is $R = 300$ mm. Based on the above values of the parameters, this antenna can produce the presented three LCP OAM modes and the other three RCP OAM modes from 1.9GHz to 3GHz.

III. SIMULATED RESULTS AND DISCUSSION

The simulation is carried out with CST microwave studio [30]. The reflection coefficients of the eight wave ports are shown in Fig. 2, in which the values of the whole curves are almost below than -10dB in the frequency range 1.9-3GHz, and there exist less differences among these curves, showing a good performance of this antenna.

In order to investigate the radiation characteristics of the proposed antenna, the electric field distributions of the six generated modes in 1.9-3GHz are simulated and
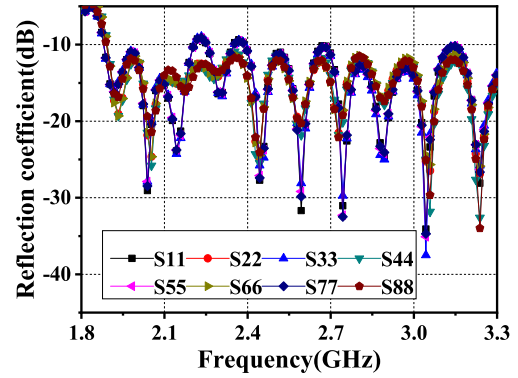

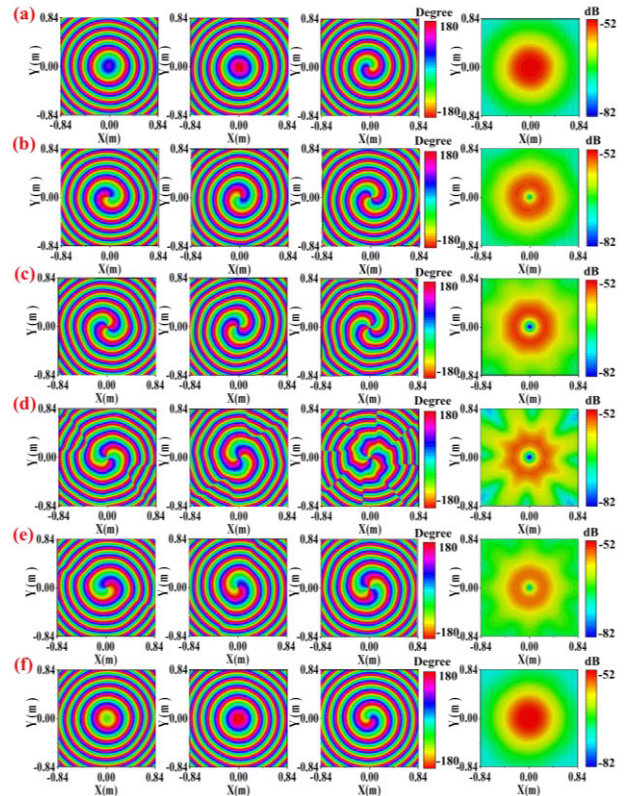**FIGURE 2.** The reflection coefficients of the eight wave ports.

FIGURE 3. The simulated intensities of the total radiated electric field and the phase distributions of x-/y-/z-components at 2.45GHz with the different modes of (a) LCP l = 0, (b) LCP l = 1, (c) LCP l = 2, (d) RCP l = −2, (e) RCP l = −1 and (f) RCP l = 0, respectively.

discussed. As a representative of them, the intensities of the total radiated electric fields and the phase distributions of x-/y-/z-components of electric fields at 2.45GHz are shown in Fig. 3. The observation plane with 1.68m × 1.68m is 0.4m away from the antenna. It is apparent that the phase patterns have the anticlockwise rotations with 0, -2π, -4π phase changes and clockwise rotations with 4π, 2π and 0 phase changes around one circle in Figs. 3(a-f), respectively. Meanwhile, the phases of y-component are 90degree ahead of that of x-component in Fig. 3(a-c), which is opposite to that in Figs. 3(d-f). Therefore, the modes of the vortex waves
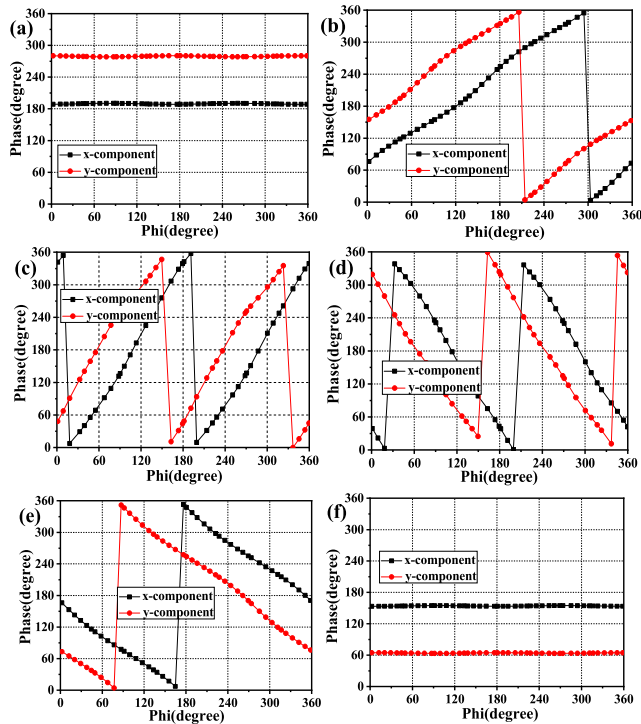
FIGURE 4. The spatial phase distributions of x and y-components of the electric fields at 2.45GHz (a-c) LCP l = 0, 1, 2 (d-f) RCP l = −2, −1, 0, respectively.

FIGURE 5. The axial ratios of vortex wave with different OAM modes at 2.45GHz in (a) E-plane and (b) H-plane, respectively.

FIGURE 6. The simulated intensities of the total radiated electric field and the phase distributions of x-/y-/z-components with the same mode of LCP l = 1 at (a) 2GHz (b) 2.45GHz and (c) 3GHz, respectively.

are LCP $l = 0, 1, 2$ in Figs. 3(a-c) and RCP $l = -2, -1, 0$ in Figs. 3(d-f), respectively. And all of the phase shifts for the z-component are 2π more than the phase shifts of x-/y-components of LCP vortex waves, while -2π less than the phase shifts of x-/y-components of RCP vortex waves, which means the generated vortex waves are circularly polarized. The reasons are summarized as follows: firstly, the z-component contains the spin orbital angular (SAM) and OAM, but x-/y- component only include OAM; secondly, both of the SAM and OAM are determined by the same traveling current. Once the turn of the traveling current is determined, polarizations and OAM modes are determined simultaneously and in line with the turn of the traveling current. Therefore, left-hand circular polarization is bound to positive OAM mode while right-hand circular polarization is bound to negative OAM mode. In addition, except the modes of $l = 0$ (a bright spot in the center), the intensities of the electric field exhibit doughnut shapes with nulls in the center, which are the important characteristics of the vortex waves with different OAM modes. The intensity and phase mutation of mode $l = -2$ may be caused by the loss and the phase unevenness of the reverse current.

For further verifications, the spatial phase distributions of the x-/y-components of the electric fields at 2.45GHz are calculated from the field distributions on the circles corresponding to the magnitude maximum. As shown in Fig. 4, one can see that the phases of y-components are 90degree ahead (in Figs. 4(a-c)) and lag (in Figs. 4(d-f)) that of x-component, respectively, corresponding to the LCP and
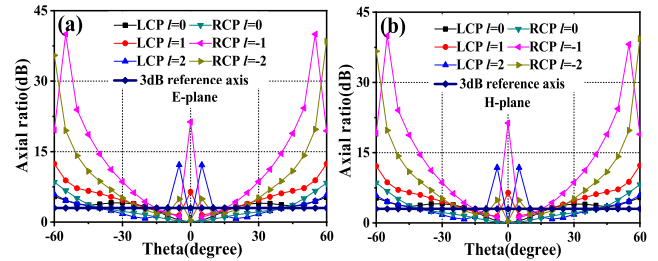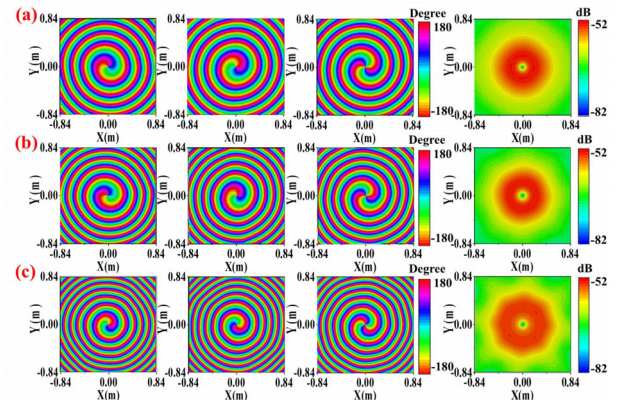
RCP vortex waves. Since the results of the phase changes illustrated in Fig. 4 agree well with those in Fig. 3, where spiral shapes are observed for LCP $l = 0, 1, 2$ and RCP $l = -2, -1, 0$, the fact that this antenna can generate vortex waves of six modes has been proven again. The circular polarization characteristics of vortex waves with different OAM modes at 2.45GHz can also be proven by the axial ratio distributions in E and H plane, as shown in Figs. 5(a) and (b), respectively. Due to the situation that the RCP vortex waves are formed by radiations from reverse currents reflected at the origins of arms and there may exist some losses in reverse currents, the axial ratios of RCP vortex waves are worse than that of LCP vortex waves. Fortunately, most of the axial ratios in low theta angles are still low than 3dB and the axial ratio distributions in E-plane is almost same to that in H-plane, which means the good performances of circular polarization characteristics in low-theta angles and the whole phi angles.

In order to consider the influence of the frequencies on field distributions, the vortex waves with the six modes have been simulated and analyzed in 1.9-3GHz. The intensity distributions of the total radiated electric field and the phase distributions of x-/y-/z-components of electric fields with the modes of LCP $l = 1$ at 2GHz, 2.45GHz and 3GHz are presented in Figs. 6(a-c), respectively. It can be seen that the phase changes of x-/y-components in one turn are all 2π, corresponding to one-OAM-mode waves. The intensities of the electric field exhibit doughnut shapes with nulls in the
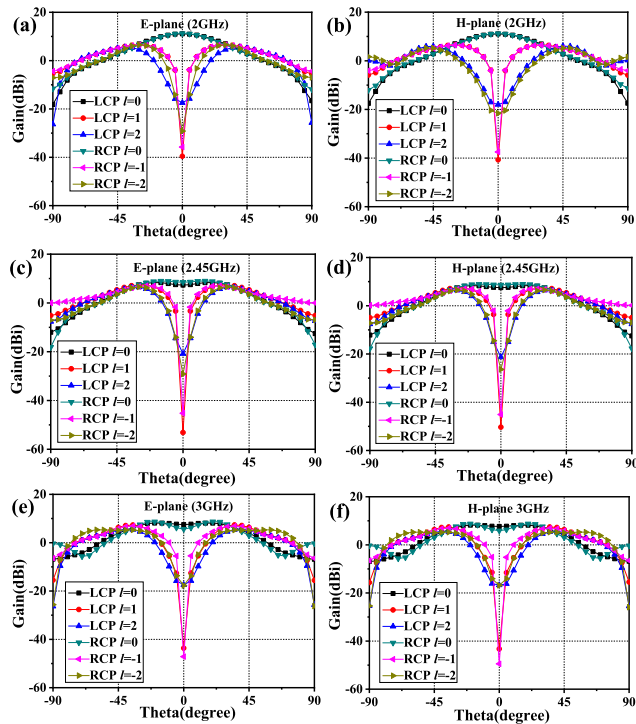
FIGURE 7. The radiation patterns of the generated vortex waves carrying different OAM modes in (a) E-plane and (b) H-plane at 2GHz, (c) E-plane and (d) H-plane at 2.45GHz, (e) E-plane and (f) H-plane at 3GHz.

TABLE 2. The far-field radiation characteristics of voertex wavs with different oam modes at different frequencies.

Frequency	*OAM mode	E plane		H plane	
		*DA (degree)	3dB *AW (degree)	DA (degree)	3dB AW (degree)
2	RCP-2	50	29.1	50	29.2
	RCP -1	30	42.1	30	42.2
	*RCP0	0	22.7	0	22.6
	*LCP 0	0	25.1	0	24.9
	LCP 1	30	41.1	30	41.1
	LCP 2	45	30.9	45	30.9
2.45	RCP -2	30	27.3	30	27.3
	RCP -1	25	36.7	25	36.7
	RCP 0	15	37.2	15	37.2
	LCP 0	20	39.9	20	39.9
	LCP 1	30	35.5	30	35.5
	LCP 2	30	33.3	30	33.2
3	RCP -2	55	54.4	55	54.4
	RCP -1	35	35.1	35	35.1
	RCP 0	20	36.3	30	36.2
	LCP 0	20	40.3	15	40.3
	LCP 1	35	30.4	35	30.4
	LCP 2	40	36.6	40	36.6

*OAM: orbital angular momentum *RCP: right-hand circularly polarized
*LCP: left-hand circularly polarized *DA: direction angle *AW: angular width
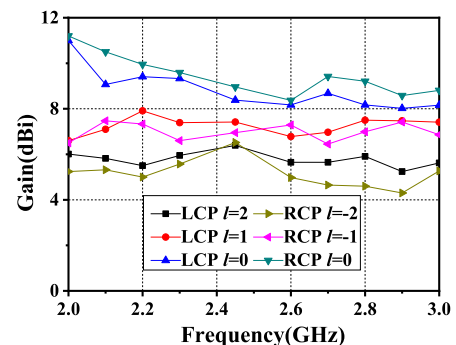

FIGURE 8. The maximum gains of the vortex wave with different OAM modes in frequency range of 2-3GHz.

center and the region with low field intensity becomes wider with the increase of frequency. The reason is that with the same observation distance of 0.4m, the ratio between the observation distance and wavelength will change larger with the increase of frequency, which results in a relative longer propagation distance and a relative larger transmission loss. Therefore, the generated vortex wave will have a larger beam divergence angle, which leads to the wider region of low field intensity.

In order to verify the far-field radiation characteristics of the proposed antenna, the 2-D radiation patterns in the E and H planes with different OAM modes at 2GHz, 2.45GHz and 3GHz are shown in Figs. 7(a-f), respectively. In addition, for more clear understand, TABLE 2 gives the corresponding direction angles and 3dB angular widths of these generated vortex waves, respectively. Although the direction angles of the main lobe and 3dB angular widths change a little with the increase of frequency, these angles increase relatively faster with the increasing of $|l|$, which is the radiation feature of the OAM waves. Meanwhile, these angles are identical in E and H-plane, which also shows the good performance of the azimuthal circular polarization characteristics. Due to the influences among the eight metal coaxial lines, the maximum gain is not at 0 degree at the frequencies of 2.45 and 3GHz, but the amplitude at 0 degree is just a little smaller than the maximum amplitude, which is still acceptable.

In general, the gains of traditional planar antennas are relatively low, hindering their relevant applications. Fortunately, the proposed antenna has higher gains compared with the

traditional planar antennas. The reason is that it is fed by eight waveguide ports, with the coupling of radiation fields from the eight ports, which are similar to that of the antenna array, higher gains can be obtained. The maximum gains of the vortex wave with different OAM modes in frequency range of 2-3GHz are obtained from the simulation, as shown in Fig.8. The maximum gains decrease with the increase of $|l|$ while have few changes with the increase of frequency. In fact, the higher $|l|$, the lower the maximum value of $|J_l(ka\sin\theta)|$ which represents the magnitude of the angular field component in formula (1a), so the lower gain of the antenna. Moreover, the whole gains are in the range of 4.3-11.2dBi, which are still higher than these of the conventional planar antennas.

IV. FABRICATION AND MEASUREMENT OF THE ASA
To verify the theoretical and simulated results of the proposed antenna, a prototypes has been fabricated and measured
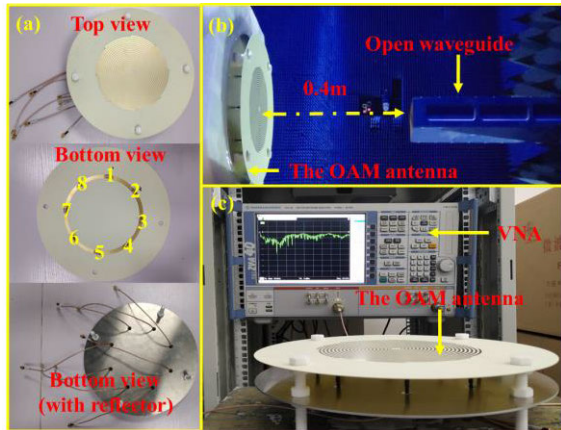
FIGURE 9. (a) Prototype of the fabricated antenna, (b) the near field test scenario, (c) the reflection coefficients test scenario.

FIGURE 10. The experimental reflection coefficients of the eight wave ports.

accordingly. Prototype of the fabricated antenna, the near-field and reflection coefficients test scenario are shown in Figs. 9(a-c), respectively. The ports 1, 2, 3, 4, 5, 6, 7 and 8 connect with eight coaxial lines of 50Ω, which are corresponding to these eight ports in Fig. 2(b). The reflection coefficients of the eight ports and near field distributions of ASA are measured by a vector network analyzer (VNA, Rohde & Schwarz, ZVA 40), in which an open waveguide is used as the detecting antenna. In addition, an eight-way power divider and an eight-way phase shift are used to feed the ASA for measuring the near-field distributions. In the same way, seven loads of 50Ω serve as the impedance matching apparatus when measuring reflection coefficients. The sampling plane paralleling in the x–y plane is 0.4m away from OAM antenna along the z-axis. The size of the sampling plane is 1.68m × 1.68m, and the number of the sampling points is 31 × 31.

The experimental reflection coefficients of the eight ports are presented in Fig. 10, all the lines are below than −10dB in the frequency range of 1.9-3GHz, and each is almost the same to the other, which agree well with the simulated ones. The experimental intensity distributions of the total near field and the phase distributions of x-/y-component of near field with the OAM modes of LCP $l = 0, 1, 2$ and RCP $l = -2, -1, 0$ at 2.45GHz are presented in Figs. 11(a-f), respectively. The intensity distributions satisfy the "donut shape" and the phase distributions satisfy the "spiral shape", which both shows their good performance. In addition, the null of the intensity distributions, the phase shifts and the directions of phase rotation are consistent with simulation ones, which also demonstrate the circular polarization and OAM characteristics of the generated vortex waves. Therefore, the vortex waves with the same circular polarization and OAM modes to that of simulations can be generated.

In general, following the Huygens principle, the measured data in the near field can be transformed into the far field [31]

$$\psi(r') = \oint_S \left[G(r, r')\nabla\psi(r) - \psi(r)\nabla G(r, r') \right] \cdot \hat{n} dS \quad (3)$$
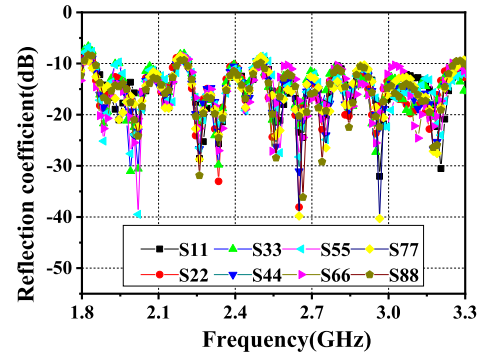
where $G(r, r')$ is the Green function, $\psi(r')$ and $\psi(r)$ denote the potential functions in the far field and near field, respectively. Through the inverse Fourier transform, the experimental far-field 3D intensity and phase patterns at 2.45GHz with the different OAM modes of LCP $l = 0, 1, 2$ and RCP $l = -2, -1, 0$ are displayed in Figs. 12(a-b), respectively. With the transmission of the vortex waves, the far-field intensity and phase distributions seem to grow better than these of near field, and their distributions are more in line with the characteristics of the corresponding vortex waves, which demonstrates their good radiation performances.

In order to obtain the far-field gains, the inverse Fourier transform are used again, and the experimental radiation patterns in the H and E planes of vortex waves at 2.45GHz with different OAM modes of LCP $l = 0, 1, 2$ and RCP $l = 0, -1, -2$ are shown in Figs 12(c-d), respectively. The fields in H and E planes are almost same to the other and the maximum gains of in E plane with different OAM modes of LCP $l = 0, 1, 2$ and RCP $l = 0, -1, -2$ are 10.02dBi, 8.52dBi, 7.73dBi, 9.38dBi, 8.25dBi and 8.45dBi, respectively. The corresponding directional angles are −0.1deg, −23.24deg, 43.32deg, −1.76deg, 23.59deg and −42.27deg, respectively.

Meanwhile, in order to further prove the advantages of the proposed antenna, TABLE 3 presents the performance comparisons of this work with other recently reported OAM-generating antennas. Compared with the existing antennas in [18]–[21], [25], the proposed antenna can produce multiple OAM modes over a respectable frequency band while maintaining a higher gain of the radiated field. As for the antennas in [21]–[23], they can only generate different OAM modes in different frequency ranges, not all of the OAM modes over all the frequency range. Last but not the least, the proposed antenna structure is much smaller and lower cost than that of 16 horn array in [28] while keeping multiple OAM modes over a respectable frequency band.

However, there has been a large debate between OAM multiplexing technology and other space diversity techniques [32], [33], from which the capacity of OAM system is not larger than other space diversity techniques. The larger divergence angle and smaller gain of the vortex waves, will greatly decrease the SNR of the signal in long distance
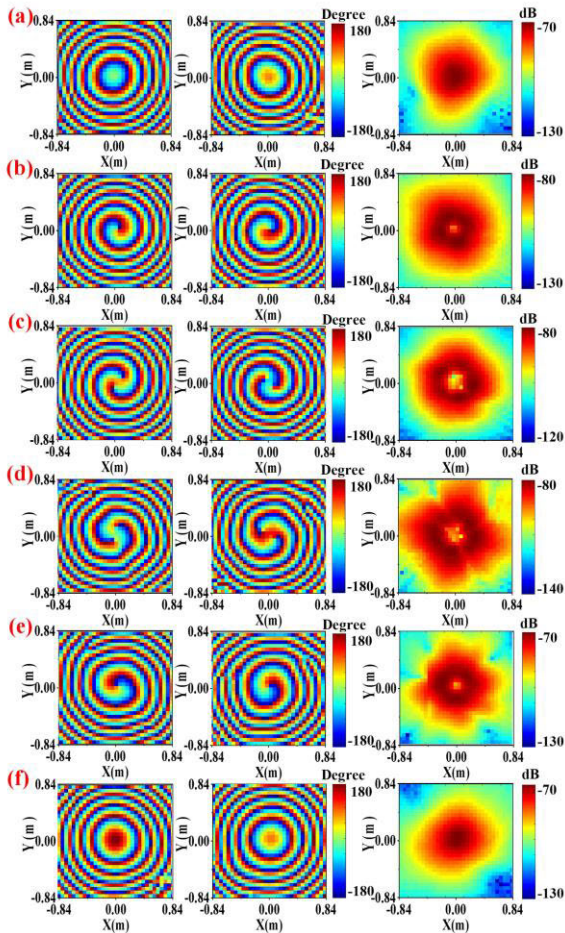
FIGURE 11. The experimental intensity distributions of the total near field and the phase distributions of x-component and y-component of near field at 2.45GHz with the OAM modes of (a-c) LCP l = 0, 1, 2 and (d-f) RCP l = −2, −1, 0, respectively.
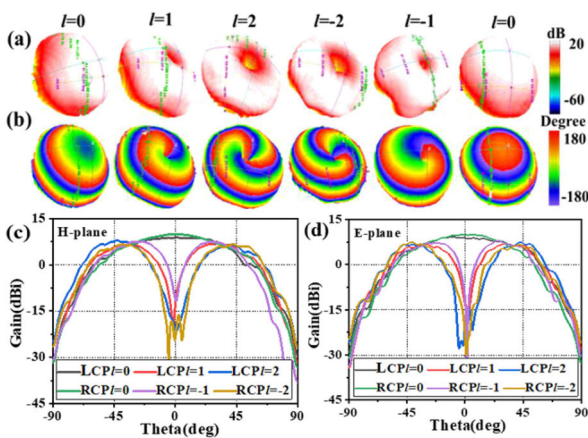

FIGURE 12. The experimental far-field (a) 3D intensity and (b) 3D phase patterns, and radiation patterns in (c) H plane and (d) and E plane at 2.45GHz with the different OAM modes of LCP l = 0, 1, 2 and RCP l = −2, −1, 0, respectively.

transmission, hindering the improvement of communication capacity. Fortunately, there are some methods that can suppress this problem to some extent, such as adding metal cavity

TABLE 3. Performance comparisons with reported OAM antennas.

*Ref	Antenna Structure	Size(λ_0)	*BW (GHz)	OAM Modes	Gain (dBi)
[18]	Concentric patches	Φ2.26	5.65	1,-2	*N.A
[19]	Conical conformal MP	Φ3.63×0.22	2.4	±1 ±2	6.6 N.A
[20]	Cavity+ slot+ Horn	Φ4.12	10	2,3,4	3.71
[21]	Cavity+ three-dimensional helical	Φ0.51×0.13 Φ1.03×0.26 Φ1.63×0.41	0.76 1.55 2.45	0 1 2	<4.55
[22]	*MP + cavity	Φ2.60×0.80 Φ3.47×1.07 Φ4.16×1.28	3 4 4.8	±1 ±2 ±3	6.7~10
[23]	MP	N.A	1.3-3.25 3.45-6.1 6.25-10	1 2 3	N.A
[25]	Equiangular spiral antenna	Φ3.00×0.57	3	1 3 5	6.94 6.76 5.49
[28]	16 horn array	Φ9.9	8-12	-7~7	N.A
Our work	MP	Φ2.45	1.9-3	LCP 0,1,2 RCP 0,-1,-2	4.5~11.2

*Ref: reference, *MP: microstrip-patch *BW: bandwidth *LCP: left-hand circularly polarized *RCP: right-hand circularly polarized, *N.A: not available.

(the references [21], [22] and adding metal parabolic reflector [20]. Meanwhile, the dissymmetry of field distributions influences the purity of OAM modes and then affects the communication capacity [33]. Therefore, the consistency and accuracy of the fed intensity and phase should be enhanced to produce symmetrical field distributions.

V. CONCLUSION

An eight-arm ASA is proposed to generate multiple OAM modes in an enough frequency range of 1.9-3GHz. The designed patch is eight-arm metal right-hand spiral line with outer-fed ports at the end of line. Based on the incident and reflected currents theory, the vortex waves with OAM modes of LCP l = 0, 1, 2 and RCP l = 0, −1, −2 can be generated in frequency range of 1.9-3GHz by changing the fed phases of the eight ports and controlling the radius of the antenna arm. In addition, simulated and experimental results both demonstrate the proposed antenna can produce the six high-quality vortex waves. The smaller structure, higher gain, larger frequency bandwidth as well as multiple OAM modes of this antenna are also proven by the comparisons in TABLE 3.

REFERENCES

[1] L. Allen, M. W. Beijersbergen, R. J. C. Spreeuw, and J. P. Woerdman, "Orbital angular momentum of light and the transformation of Laguerre–Gaussian laser modes," *Phys. Rev. A, Gen. Phys.*, vol. 45, no. 11, pp. 8185–8189, Jun. 1992.

[2] C. Kai, P. Huang, F. Shen, H. Zhou, and Z. Guo, "Orbital angular momentum shift keying based optical communication system," *IEEE Photon. J.*, vol. 9, no. 2, pp. 1–10, Apr. 2017.

[3] M. Padgett and L. Allen, "Light with a twist in its tail," *Contemp. Phys.*, vol. 41, no. 5, pp. 275–285, Sep. 2000.

[4] Y. Li, Z. Guo, and S. Qu, "Living cell manipulation in a microfluidic device by femtosecond optical tweezers," *Opt. Lasers Eng.*, vol. 55, pp. 150–154, Apr. 2014.

[5] L. Zhu, Z. Guo, Q. Xu, J. Zhang, A. Zhang, W. Wang, Y. Liu, Y. Li, X. Wang, and S. Qu, "Calculating the torque of the optical vortex tweezer to the ellipsoidal micro-particles," *Opt. Commun.*, vol. 354, pp. 34–39, Nov. 2015.

[6] G. Zhong-Yi, Q. Shi-Liang, S. Zheng-He, and L. Shu-Tian, "Superposition of orbital angular momentum of photons by a combined computer-generated hologram fabricated in silica glass with femtosecond laser pulses," *Chin. Phys. B*, vol. 17, no. 11, pp. 4199–4203, Nov. 2008.

[7] Z. Wang, M. I. Dedo, K. Guo, K. Zhou, F. Shen, Y. Sun, S. Liu, and Z. Guo, "Efficient recognition of the propagated orbital angular momentum modes in turbulences with the convolutional neural network," *IEEE Photon. J.*, vol. 11, no. 3, Jun. 2019, Art. no. 7903614.

[8] Z. Guo, Z. Wang, M. I. Dedo, and K. Guo, "The orbital angular momentum encoding system with radial indices of Laguerre–Gaussian beam," *IEEE Photon. J.*, vol. 10, no. 5, pp. 1–11, Oct. 2018.

[9] B. Thidé, H. Then, J. Sjöholm, K. Palmer, J. Bergman, T. D. Carozzi, Y. N. Istomin, N. H. Ibragimov, and R. Khamitova, "Utilization of photon orbital angular momentum in the low-frequency radio domain," *Phys. Rev. Lett.*, vol. 99, no. 8, Aug. 2007, Art. no. 087701.

[10] S. Mohaghegh Mohammadi, L. K. S. Daldorff, J. E. S. Bergman, R. L. Karlsson, B. Thide, K. Forozesh, T. D. Carozzi, and B. Isham, "Orbital angular momentum in radio—A system study," *IEEE Trans. Antennas Propag.*, vol. 58, no. 2, pp. 565–572, Feb. 2010.

[11] F. Tamburini, E. Mari, A. Sponselli, B. Thidé, A. Bianchini, and F. Romanato, "Encoding many channels on the same frequency through radio vorticity: First experimental test," *New J. Phys.*, vol. 14, no. 3, Mar. 2012, Art. no. 033001.

[12] B. Allen, A. Tennant, E. Chatziantoniou, and Q. Bai, "Wireless data encoding and decoding using OAM modes," *Electron. Lett.*, vol. 50, no. 3, pp. 232–233, Jan. 2014.

[13] G. Guo, W. Hu, and X. Du, "Electromagnetic vortex based on the radar target imaging," (in Chinese), *J. Nat. Univ. Defense Technol.*, vol. 35, no. 6, pp. 71–76, Dec. 2013.

[14] K. Liu, Y. Cheng, Z. Yang, H. Wang, Y. Qin, and X. Li, "Orbital-angular-momentum-based electromagnetic vortex imaging," *IEEE Antennas Wireless Propag. Lett.*, vol. 14, pp. 711–714, Mar. 2015.

[15] L. Li and F. Li, "Beating the Rayleigh limit: Orbital-angular-momentum-based super-resolution diffraction tomography," *Phys. Rev. E, Stat. Phys. Plasmas Fluids Relat. Interdiscip. Top.*, vol. 88, no. 3, pp. 033205-1–033205-6, Sep. 2013.

[16] Q. Fan, "Super-resolution imaging of high-contrast target in electromagnetic inverse scattering," (in Chinese), *Acta Phys. Sinica*, vol. 67, no. 14, pp. 133–144, 2018.

[17] G. A. Turnbull, D. A. Robertson, G. M. Smith, L. Allen, and M. J. Padgett, "The generation of free-space Laguerre–Gaussian modes at millimetre-wave frequencies by use of a spiral phaseplate," *Opt. Commun.*, vol. 127, pp. 183–188, Jun. 1996.

[18] Z. Zhang, S. Xiao, Y. Li, and B.-Z. Wang, "A circularly polarized multi-mode patch antenna for the generation of multiple orbital angular momentum modes," *IEEE Antennas Wireless Propag. Lett.*, vol. 16, pp. 521–524, 2017.

[19] F. Shen, J. Mu, K. Guo, and Z. Guo, "Generating circularly polarized vortex electromagnetic waves by the conical conformal patch antenna," *IEEE Trans. Antennas Propag.*, vol. 67, no. 9, pp. 5763–5771, Sep. 2019.

[20] W. Zhang, S. Zheng, X. Hui, Y. Chen, X. Jin, H. Chi, and X. Zhang, "Four-OAM-mode antenna with traveling-wave ring-slot structure," *IEEE Antennas Wireless Propag. Lett.*, vol. 16, pp. 194–197, 2017.

[21] F. Shen, J. Mu, K. Guo, S. Wang, and Z. Guo, "Generation of continuously variable-mode vortex electromagnetic waves with three-dimensional helical antenna," *IEEE Antennas Wireless Propag. Lett.*, vol. 18, no. 6, pp. 1091–1095, Jun. 2019.

[22] L. Wang, H. Chen, K. Guo, F. Shen, and Z. Guo, "An inner- and outer-fed dual-arm archimedean spiral antenna for generating multiple orbital angular momentum modes," *Electronics*, vol. 8, no. 2, p. 251, 2019.

[23] F. Mao, F. Huang, T. Li, J. Zhang, and C. Yang, "Broadband generation of orbital angular momentum carrying beams in RF regimes," *Prog. Electromagn. Res.*, vol. 160, pp. 19–27, 2017.

[24] Z. Guo, Z. Li, J. Zhang, K. Guo, F. Shen, Q. Zhou, and H. Zhou, "Review of the functions of Archimedes' spiral metallic nanostructures," *Nanomaterials*, vol. 7, no. 11, p. 405, 2017.

[25] Y. Yang, K. Guo, F. Shen, Y. Gong, and Z. Guo, "Generating multiple OAM based on a nested dual-arm spiral antenna," *IEEE Access*, vol. 7, pp. 138541–138547, 2019.

[26] Z. Yin, Q. Zheng, K. Guo, and Z. Guo, "Tunable beam steering, focusing and generating of orbital angular momentum vortex beams using high-order patch array," *Appl. Sci.*, vol. 9, no. 15, p. 2949, 2019.

[27] L. Junfeng, L. Shuo, F. Xiaojian, and C. Tiejun, "Terahertz information metamaterials and metasurfaces," (in Chinese), *J. Radar*, vol. 7, no. 1, pp. 46–55, 2018.

[28] K. Liu, H. Liu, Y. Qin, Y. Cheng, S. Wang, X. Li, and H. Wang, "Generation of OAM beams using phased array in the microwave band," *IEEE Trans. Antennas Propag.*, vol. 64, no. 9, pp. 3850–3857, Sep. 2016.

[29] A. Mehrabani and L. Shafai, "Polarisation reconfigurable, centre-fed, and low-profile archimedean spiral antennas with unidirectional broadside patterns," *IET Microw., Antennas Propag.*, vol. 11, no. 5, pp. 726–731, Apr. 2017.

[30] CST Studio Suite 2016. *CST Computer Simulation Technology AG*. Accessed: Sep. 13, 2019. [Online]. Available: https://www.cst.com

[31] W. L. Stutzman and G. A. Thiele, *Antenna Theory and Design*, 3rd ed. New York, NY, USA: Wiley, 2012.

[32] O. Edfors and A. J. Johansson, "Is orbital angular momentum (OAM) based radio communication an unexploited area?" *IEEE Trans. Antennas Propag.*, vol. 60, no. 2, pp. 1126–1131, Feb. 2012.

[33] R. Gaffoglio, A. Cagliero, G. Vecchi, and F. P. Andriulli, "Vortex waves and channel capacity: Hopes and reality," *IEEE Access*, vol. 6, pp. 19814–19822, 2018.

[34] A. Cagliero, "Symmetry breaking in UCA-based vortex waves," *J. Phys. Commun.*, vol. 2, no. 9, 2018, Art. no. 095012.

• • • •